https://doi.org/10.5194/egusphere-2025-2561
Preprint. Discussion started: 16 September 2025

Operational calibration of a fully polarimetric radiometer for stratospheric temperature retrievals

Witali Krochin[1,2], Axel Murk[1,2], Andres Luder[1], and Gunter Stober[1,2]

[1]Institute of Applied Physics, University of Bern
[2]Oeschger Center for Climate Change Research, University of Bern

Correspondence: Witali Krochin (witali.krochin@unibe.ch)

Abstract. The oxygen emission band at 60 GHz is a commonly used frequency band for atmospheric temperature sounding. The oxygen fine structure emission lines used for retrievals of the temperature in the stratosphere and mesosphere are affected by the Zeeman effect which has a characteristic influence on the spectral shape of different polarization states. As a consequence of this effect, a V-Stokes component is generated, indicating symmetry breaking between right and left circular polarized radiation. In this study, we present the full-rank Stokes vector of the fine structure emission lines at 53.067 GHz and 53.596 GHz, measured with a fully polarimetric radiometer. We discuss the advantages of the fully polarimetric approach compared to single-polarization observations for temperature sounding by comparing both simulations and observations. Finally, we present an operational calibration method and show calibrated spectra of the four components of the Stokes polarization vector and a continuous series of the retrieved temperature profiles.

1 Introduction

Microwave radiometry is a common technique for continuously monitoring atmospheric parameters such, water vapour, ozone, temperature, and other trace gases. In addition to the two linear polarizations, fully polarimetric instruments measure the 3rd and 4th components of the Stokes vector, providing a pathway to obtain the circular polarization which is independent of the rotation of the polarization plane by the Faraday effect or instrument optics. So far, it was shown that the fully polarimetric technique can be used to monitor the ocean wind vector (Laursen and Skou (2001); Piepmeier and Gasiewski (2001a, b)). Resolving all four Stokes components is a challenge for calibration, hence, the polarimetric approach has not yet been used to retrieve atmospheric temperature profiles.

Atmospheric temperature profiles are retrieved from measurements of the oxygen band at 60 GHz. To retrieve tropospheric temperatures, several broadband channels are used to cover the left wing of the oxygen band. Making use of a high-resolution spectrometer, fine structure emission lines can be resolved to retrieve temperatures in the stratosphere and mesosphere (Stähli et al. (2013)). Due to the coupling of molecular oxygen to the Earth's magnetic field, the Zeeman effect has to be taken into account when calculating the absorption coefficients from rotational transitions, introducing additional challenges in the radiative transfer calculations. The resulting Zeeman broadening leads to a natural upper altitude limit for temperature retrievals at

https://doi.org/10.5194/egusphere-2025-2561
Preprint. Discussion started: 16 September 2025

altitudes where it dominates over the pressure broadening (Krochin et al. (2022a)). The coupling to the magnetic field breaks the symmetry for transitions in rotational energy and the rotational axis and generates a non-zero contribution in all 4 components of the Stokes vector. Therefore, additional information content can be obtained with fully polarimetric measurements compared to single-polarization measurements.

TEMPERA-C is a fully polarimetric ground-based radiometer designed to measure two fine structure oxygen emission lines at 53.067 GHz and 53.596 GHz Krochin et al. (2022b). For a test campaign, the instrument was deployed at the Jungfraujoch high-altitude research station (3571 m.a.s.l) from March to November 2024 and performed continuous temperature soundings. For the campaign, an operational calibration method was developed by measuring cross-talk coefficients in the laboratory using the assumption that these coefficients stay constant during the campaign. Instrument gain and noise, which are more variable parameters, were calibrated frequently on-site with built-in noise diodes and an ambient load calibration target. From the measured Stokes vector, the right and left circular polarizations were computed and inverted into temperature profiles by using the atmospheric radiative transfer simulator ARTS (Buehler et al. (2005); Eriksson et al. (2011); Buehler et al. (2018, 2024)).The Zeeman algorithm implemented in ARTS (Larsson et al. (2014, 2019)) is crucial for radiative transfer calculations above the troposphere. In this study, we present results of the instrument calibration and the temperature retrievals from the test campaign.

2 Zeeman effect in atmospheric oxygen

Due to unpaired electrons in the bonding orbit, the oxygen molecule carries a magnetic dipole moment and couples to the Earth's magnetic field. The coupling leads to Zeeman splitting of rotational energy states. In the observed frequency band, this results in a broadening of the lineshape around the center. The Zeeman line-broadening causes an upper altitude limit for temperature retrievals using the 60 GHz oxygen band because it starts to dominate over the pressure broadening at mesospheric altitudes. The line broadening caused by the Zeeman effect on the fine structure lines in the 60 GHz oxygen band was investigated in Navas-Guzmán et al. (2015), measuring the lineshape with a linear polarized receiver and a high-resolution spectrometer at different azimuth angles. Retrievals of atmospheric temperature profiles from ground-based measurements, including the Zeeman effect in the forward model, were published in Krochin et al. (2022a). The upper altitude limit reached with this algorithm was about 50 km. It was argued in Krochin et al. (2022b) that, in contrast to single polarized measurements, this limit can be increased by measuring multiple polarization components of the Zeeman broadened emission lines due to the increased information content, specifically in the characteristically shaped V-Stokes component. In this manuscript, we perform a direct comparison of the different retrieval algorithms to confirm the information gain, although the impact appears to be smaller than expected (see 7).

Based on the vertical and horizontal polarization (v,h), the 4-component Stokes vector is defined as

https://doi.org/10.5194/egusphere-2025-2561
Preprint. Discussion started: 16 September 2025

$$I = |E_v|^2 + |E_h|^2 \tag{1}$$

$$Q = |E_v|^2 - |E_h|^2 \tag{2}$$

$$U = 2\Re\{\langle E_v E_h^* \rangle\} \tag{3}$$

$$V = -2\Im\{\langle E_v E_h^* \rangle\}. \tag{4}$$

The characteristic line shapes of the Stokes components for the emission line with center at 53.067 GHz are illustrated in 1. Simulations of the Stokes components in ARTS use the refined Zeeman split coefficients from Larsson et al. (2019). The first three Stokes components exhibit symmetric spectra around the line center, whereas the V-Stokes component is antisymmetric. The line shapes depend on the angle of the line of sight to the magnetic field lines. The maximum of the V-Stokes component is expected to be emitted parallel to the field lines and vice versa.

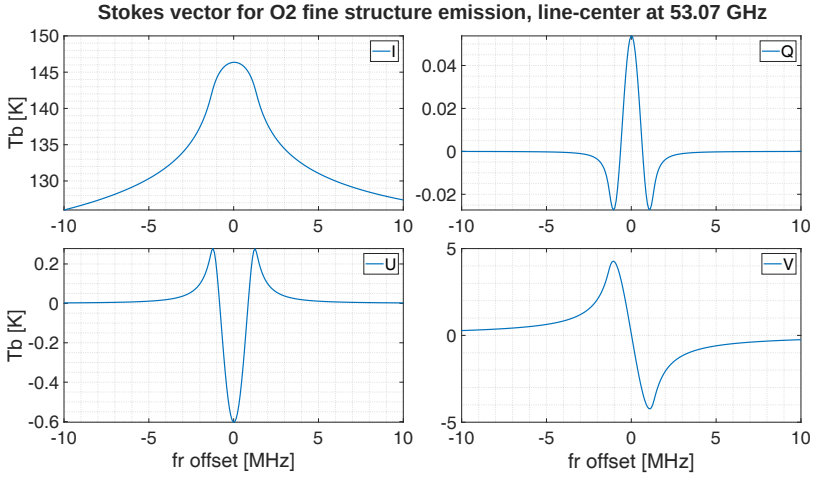

Figure 1. The four components of the Stokes vector, simulated for the Zeeman split emission line at 53.067 GHz

3 Instrument description

The electronic architecture of the front end is described in Krochin et al. (2022b). A simplified schematic is illustrated in Fig. 2. Radiation passing the horn antenna is decomposed into the linear polarization components (h, v) by the ortho mode transducer (OMT). The two orthogonally polarized signals are guided through identical receiver channels with a low noise amplifier (LNA) (7), band pass (8), and mixer (9), which share the same local oscillator. The amplified, filtered, and down-converted signals are the input of the digital correlator. The output of the digital correlator consists of a total of 8 spectra with 100 MHz bandwidth and 4096 channels. Two self-correlated components of the receiver chain h and v, as well as the imaginary and real parts of the cross-correlated signals.

https://doi.org/10.5194/egusphere-2025-2561
Preprint. Discussion started: 16 September 2025

The initial results in Krochin et al. (2022b) were obtained with an early prototype of the instrument with simplified optics. In this publication we show the results with the final optical design. It includes a corrugated feed with an ultra-gaussian antenna pattern and a measured cross-polarization below -40 dB (see Fig.5), an off-axis parabolic reflector which is designed with a full width half maximum beam width of 3.2° degrees in the far field of the instrument. A rotatable planar mirror is used to switch the direction of the beam between the hot and cold calibration targets and sky direction with an adjustable zenith angle. The rotating mirror is mounted on a linear translation stage, which is used to change the distance between the receiver and the targets by a quarter wavelength after each calibration cycle in order to mitigate the effect of standing waves. The optics were designed with the commercial software GRASP from Ticra (see Fig. 3). For the ambient temperature source, a microwave absorber was placed below the instrument. Another microwave absorber placed in a liquid nitrogen bath acts as a cold target to calibrate the noise diodes.

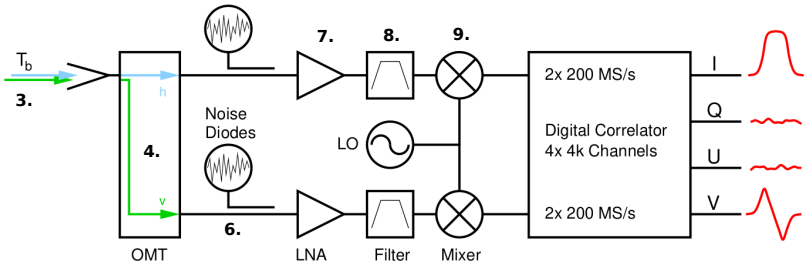

Figure 2. Simplified chart of the TEMPERA-C front-end Krochin et al. (2022b).

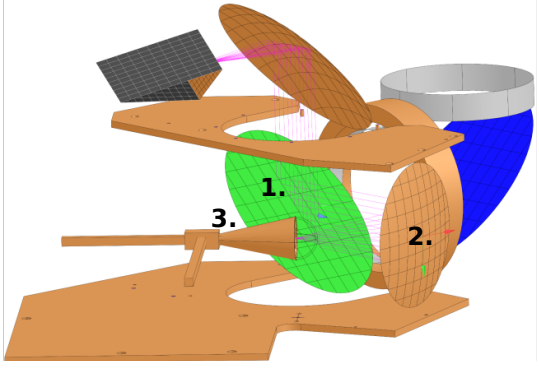

Figure 3. GRASP model of the TEMPERA-C optic with the feed-horn (3), the focusing mirror (2), and the rotating mirror (1). In addition, components of the final mounting (see. Sec. 9) are illustrated.

https://doi.org/10.5194/egusphere-2025-2561
Preprint. Discussion started: 16 September 2025

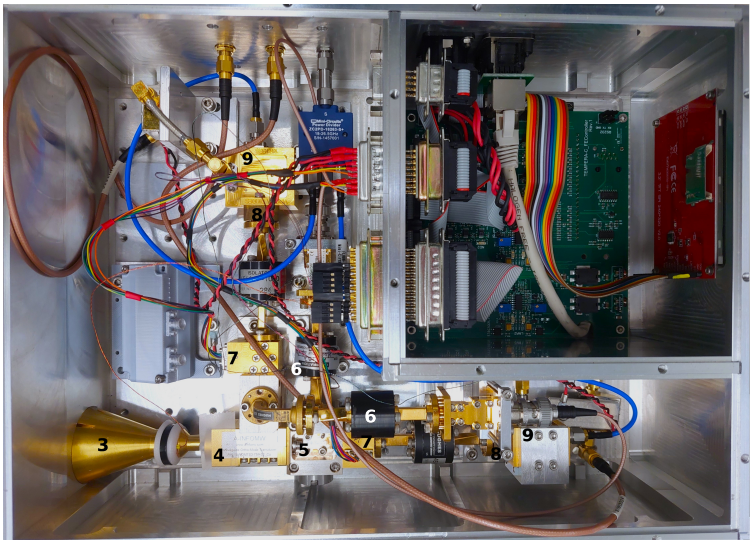

Figure 4. Interior of the TEMPERA-C front-end.

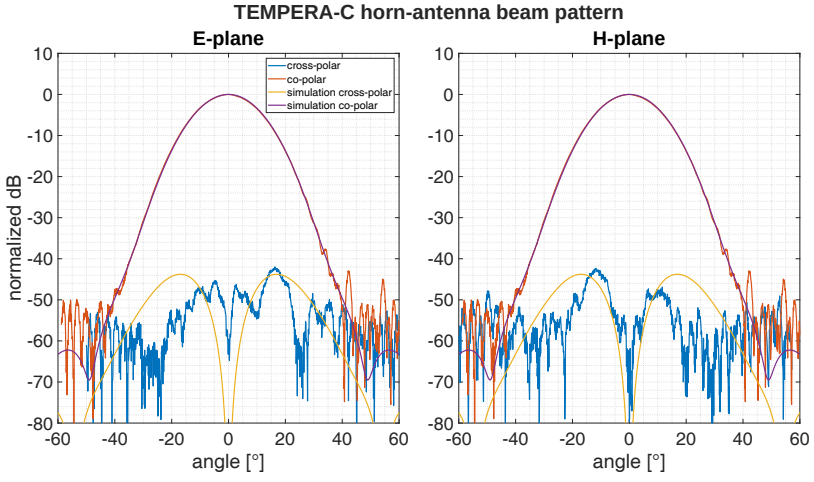

Figure 5. Measured and simulated co- and cross-polar antenna pattern of the feed horn at 53 GHz. The cross-polar field generates crosstalk between the polarization components. The measurements were performed with a linear polarized receiver.

https://doi.org/10.5194/egusphere-2025-2561
Preprint. Discussion started: 16 September 2025

4 TEMPERA-C at the Jungfraujoch high altitude research station

For a test campaign, TEMPERA-C was installed in the Sphinx observatory at the High Altitude Research Station Jungfraujoch (HFSJG). The Sphinx observatory is located at an altitude of 3571 m.a.s.l.. At this altitude, the tropospheric air mass through which radiation emitted at the stratosphere and mesosphere must propagate to reach the surface is greatly reduced compared to observations at sea level. In addition, the brightness temperature in the 60 GHz band is influenced by the water vapour continuum (see Fig. 6), which has a lower intensity due to a decreasing water vapour volume mixing ratio with altitude. It was found that the ratio between the middle atmospheric signal and the tropospheric signal amplitude increases from 1.05 to 1.2 for clear sky conditions (see Fig. 7). The relative air humidity at the time the observations were taken was 85% at the Jungfraujoch (25.03.2024) and 65% in Bern (31.03.2025). The location is therefore advantageous for ground-based observations in this frequency band to retrieve stratospheric temperature profiles. During the test campaign, the instrument was aligned to the east and had a zenith angle of 30°. Since the instrument was deployed inside one of the Sphinx laboratories, a microwave transparent window was used for the sky observations.

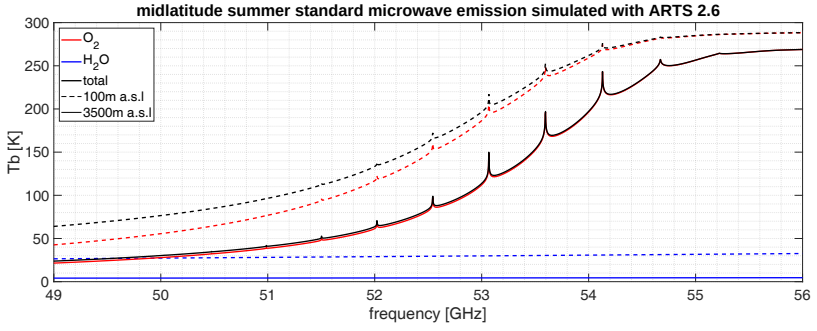

Figure 6. Left wing of the 60 GHz oxygen band as seen from ground at a zenith angle of 30°. Simulated for two sensor altitudes of 100 m a.s.l. and 3500 m a.s.l.

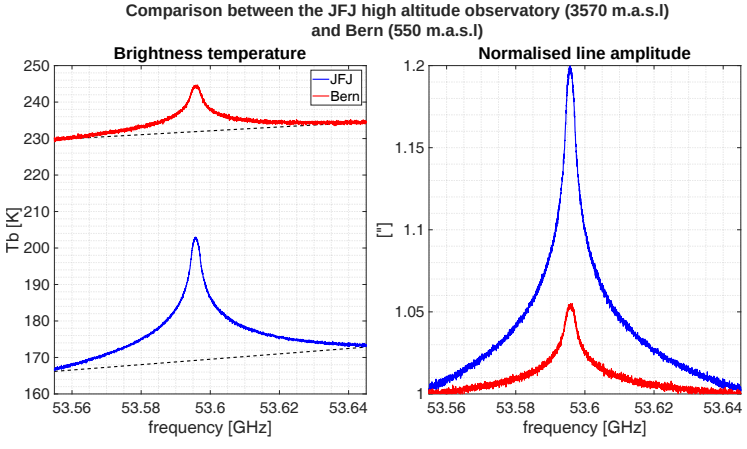

Figure 7. Comparison of calibrated TEMPERA-C measurements between Bern and the Jungfraujoch high altitude station. The illustration shows the measured fine structure emission line at 53.596 GHz in single polarization.

https://doi.org/10.5194/egusphere-2025-2561
Preprint. Discussion started: 16 September 2025

5 Calibration

5.1 The gain matrix

The calibration method is mainly based on the methods from Gasiewski and Kunkee (1993) and Lahtinen et al. (2003). An important difference is that we use a digital correlator instead of an analog correlator, which makes it possible to reduce the number of independent scans for the calibration of the full Stokes vector.

In the notation of Lahtinen et al. (2003), the brightness temperature vector is:

$$T_B = \begin{bmatrix} T_v \\ T_h \\ T_3 \\ T_4 \end{bmatrix} = \begin{bmatrix} T_v \\ T_h \\ T_{45} - T_{-45} \\ T_{cl} - T_{cr} \end{bmatrix} = \frac{\lambda^2}{k_b \eta} \begin{bmatrix} \langle |E_v|^2 \rangle \\ \langle |E_h|^2 \rangle \\ 2\Re \langle E_v E_h^* \rangle \\ 2\Im \langle E_v E_h^* \rangle \end{bmatrix}. \tag{5}$$

Here λ is the wavelength, k_b the Boltzmann constant, η the medium's impedance, and E_x the electric field for polarization x. The output vector of the spectrometer r is related to T_B through the gain matrix g, instrument noise n and a constant offset o:

$$r = \begin{bmatrix} r_a \\ r_b \\ r_3 \\ r_4 \end{bmatrix} = \begin{bmatrix} g_{vv} & g_{vh} & g_{v3} & g_{v4} \\ g_{hv} & g_{hh} & g_{h3} & g_{h4} \\ g_{3v} & g_{3h} & g_{33} & g_{34} \\ g_{4v} & g_{4h} & g_{43} & g_{44} \end{bmatrix} \begin{bmatrix} T_v \\ T_h \\ T_3 \\ T_4 \end{bmatrix} + o + n = gT_B + o + n.. \tag{6}$$

The goal of the calibration process is to find the matrix elements of g and calculate T_B by matrix inversion. In Lahtinen et al. (2003), the elements of the calibration matrix are treated as independent. Together with the 4-element instrument noise vector, this results in 20 unknown variables to determine what requires a full-rank set of Stokes vectors with a minimum number of 5 observations. Three of the five observations can be made with three different angles of the polarized grid placed with an inclination of 45°between a hot and a cold target. One additional observation is made with an unpolarized calibration target. By using a phase-retardation plate for all observations, the fifth observation is achieved by changing the angle of the retardation plate. The plate adds a phase offset between the linear polarized components depending on the angle to the polarization plane and therefore, generates a V-Stokes component, which is necessary to determine the g_{i4} and g_{4i} elements of the gain matrix.

However, the calibration method presented in this manuscript does not use a phase-retardation plate. The measurement setup corresponds to that of Gasiewski and Kunkee (1993) rather than that of Lahtinen et al. (2003). To determine the full gain matrix, we make use of two assumptions. Firstly, the gains of the diagonal elements of g are not independent. Because signals of the two receiver chains a and b are correlated digitally, the gain matrix elements g_{33}, g_{44} are functions of g_{vv}, g_{hh}. Similarly, the off-diagonal elements can be understood as functions of g_{vv}, g_{hh}, and a set of additional crosstalk parameters. Secondly,

https://doi.org/10.5194/egusphere-2025-2561
Preprint. Discussion started: 16 September 2025

we assume that the crosstalk is only generated by the antenna cross-polarization and OMT leakage and can be described by a pair of two complex crosstalk parameters c_a, c_b. The definition of the crosstalk parameters is as follows. The E-field in the linear polarized basis (v, h) in front of the antenna is:

$$E = E_h \mathbf{e}_h + E_v \mathbf{e}_v = \left(|E_h|\mathbf{e}_h + |E_v| e^{\Delta\phi i}\mathbf{e}_v\right) e^{\omega t i}. \tag{7}$$

For an ideal receiver with zero crosstalk, the off-diagonal elements of the gain matrix vanish. The signal in receiver chain a and b are simply $E_a = E_v$ and $E_b = E_h$. The calibration equation in this case is :

$$r_a = \left\langle (\mathscr{G}_a E_a)(\mathscr{G}_a E_a)^* \right\rangle + n_a = |\mathscr{G}_a|^2 \left\langle |E_v|^2 \right\rangle + n_a, \tag{8}$$

$$r_b = \left\langle (\mathscr{G}_b E_b)(\mathscr{G}_b E_b)^* \right\rangle + n_b = |\mathscr{G}_b|^2 \left\langle |E_h|^2 \right\rangle + n_b, \tag{9}$$

$$r_{3,4} = \left\langle (\mathscr{G}_a E_a)(\mathscr{G}_b E_b)^* \right\rangle + o_{3,4} = \langle \mathscr{G}_a \mathscr{G}_b^* E_v E_h^* \rangle + o_{3,4}. \tag{10}$$

Assuming that the crosstalk is resulting from the cross-polarization components of the antenna and cross-leakage of the OMT, a fraction c_a of the signal E_h enters the receiver chain a and vice versa. The signals received in chain a and b are then:

$$E_a = (E_v + c_a E_h), \tag{11}$$

$$E_b = (E_h + c_b E_v). \tag{12}$$

Leveraging the above obtained results, the calibration equation becomes:

$$r_a = \left\langle (\mathscr{G}_a E_v + \mathscr{G}_a c_a E_h)(\mathscr{G}_a E_v + \mathscr{G}_a c_a E_h)^* \right\rangle + n_a \tag{13}$$

$$= |\mathscr{G}_a|^2 \langle E_v E_v^* \rangle + |\mathscr{G}_a|^2 |c_a|^2 \langle E_h E_h^* \rangle + |\mathscr{G}_a|^2 \langle c_a^* E_v E_h^* + c_a E_v^* E_h \rangle + n_a, \tag{14}$$

$$= |\mathscr{G}_a|^2 \left[\langle E_v E_v^* \rangle + |c_a|^2 \langle E_h E_h^* \rangle + 2\Re\{\langle c_a^* E_v E_h^* \rangle\} \right] + n_a, \tag{15}$$

$$r_b = |\mathscr{G}_b|^2 \left[\langle E_h E_h^* \rangle + |c_b|^2 \langle E_v E_v^* \rangle + 2\Re\{\langle c_b^* E_h E_v^* \rangle\} \right] + n_b, \tag{16}$$

$$r_{3,4} = \left\langle (\mathscr{G}_a E_v + \mathscr{G}_a c_a E_h)(\mathscr{G}_b E_h + \mathscr{G}_b c_b E_v)^* \right\rangle + o_{3,4}, \tag{17}$$

$$= \langle \mathscr{G}_a \mathscr{G}_b^* (1 + c_a c_b^*) E_v E_h^* \rangle + \langle \mathscr{G}_a \mathscr{G}_b^* c_a E_h E_h^* \rangle + \langle \mathscr{G}_a \mathscr{G}_b^* c_b^* E_v E_v^* \rangle + o_{3,4}. \tag{18}$$

Furthermore, we introduced the symbol $\mathscr{G}$ for the complex gain, which is not of the same units as the elements of the gain matrix in Eq. (6). The relation between this notation and the notation of Eq.(6) is:

https://doi.org/10.5194/egusphere-2025-2561
Preprint. Discussion started: 16 September 2025

$$g = \begin{bmatrix} g_{vv} & g_{vh} & g_{v3} & g_{v4} \\ g_{hv} & g_{hh} & g_{h3} & g_{h4} \\ g_{3v} & g_{3h} & g_{33} & g_{34} \\ g_{4v} & g_{4h} & g_{43} & g_{44} \end{bmatrix} = \begin{bmatrix} |\mathscr{G}_a|^2 & |\mathscr{G}_a|^2|c_a|^2 & |\mathscr{G}_a|^2\Re\{c_a\} & -|\mathscr{G}_a|^2\Im\{c_a\} \\ |\mathscr{G}_b|^2|c_b|^2 & |\mathscr{G}_b|^2 & |\mathscr{G}_b|^2\Re\{c_b\} & -|\mathscr{G}_b|^2\Im\{c_b\} \\ \Re\{\mathscr{G}_a\mathscr{G}_b^* c_a\} & \Re\{\mathscr{G}_a\mathscr{G}_b^* c_b^*\} & \frac{1}{2}\Re\{\mathscr{G}_a\mathscr{G}_b^*(1+c_a c_b^*)\} & \frac{1}{2}\Im\{\mathscr{G}_a\mathscr{G}_b^*(1+c_a c_b^*)\} \\ \Im\{\mathscr{G}_a\mathscr{G}_b^* c_a\} & \Im\{\mathscr{G}_a\mathscr{G}_b^* c_b^*\} & \frac{1}{2}\Im\{\mathscr{G}_a\mathscr{G}_b^*(1+c_a c_b^*)\} & \frac{1}{2}\Re\{\mathscr{G}_a\mathscr{G}_b^*(1+c_a c_b^*)\} \end{bmatrix}. \quad (19)$$

The matrix in Eq.(19) has 8 unknowns, 4 for the real and imaginary part of the complex gain coefficients $\mathscr{G}_a$ and $\mathscr{G}_b$, and four for the crosstalk parameters c_a and c_b which are complex numbers too. The gain matrix coefficients related to the 4th Stokes component (V-Stokes) can be expressed as functions of $\mathscr{G}_a, \mathscr{G}_b, c_a, c_b$. Together with the instrument noise vector n (4 additional unknowns), the system of 20 unknown variables has been reduced to one with 12. To determine the coefficients $\mathscr{G}_a, \mathscr{G}_b, c_a, c_b$, it is sufficient to solve the system of equations generated by 4 observations of the first three Stokes components.

The assumptions leading to the equations (13)-(18) can alternatively be formulated as that the crosstalk is generated before the signal enters the LNA. Additional sources of crosstalk contributions are theoretically the path through the LO or inside the digital correlator. We verified the reliability of the assumption that crosstalk behind the LNA can be ignored by estimating the upper limit for the total cross-leakage between the receiver chains by alternately switching on the noise diode in one receiver chain and measuring the reaction in the other one. The measured reaction on the noise diode in the neighbor receiver chain was below the detection limit, providing confidence that our assumptions are valid for our receiver configuration and components. Fig 8 illustrates an upper limit for the receiver chain leakage l calculated with:

$$l_{a\to b} = \frac{r_b^{H+NDa} - r_b^H}{r_a^{H+NDa} - r_a^H} \quad (20)$$

5.2 Estimation of cross-talk parameters

The measurement setup is the same as in Lahtinen et al. (2003) (see 9).

The principal brightness T_1 and T_2 can be calculated by taking into account the parallel-polarized reflection coefficient of the polarized grid $r_\parallel$, its perpendicular-polarized transmission coefficient $t_\perp$, the absorber reflectivity r_l, and the background brightness temperature T_{BG} according to Gasiewski and Kunkee (1993) by:

$$T_1 = r_\parallel\left[(1-r_l)T_{HOT} + r_l T_{BG}\right] + \left(1-r_\parallel\right)\left[(1-r_l)T_{COLD} + r_l T_{BG}\right] \quad (21)$$

$$T_2 = t_\perp\left[(1-r_l)T_{COLD} + r_l T_{BG}\right] + (1-t_\perp)\left[(1-r_l)T_{HOT} + r_l T_{BG}\right]. \quad (22)$$

https://doi.org/10.5194/egusphere-2025-2561
Preprint. Discussion started: 16 September 2025

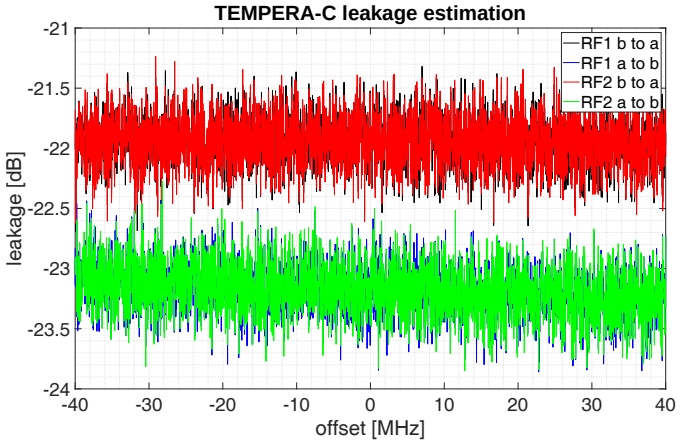

Figure 8. Upper limits of the leakage parameters, describing leakage between the receiver channels. Estimated by alternately switching on one of the two noise diodes. The RF 1 center is tuned on 53.07 GHz and the RF 2 center on 53.6 GHz. a and b are the two orthogonal polarized receivers.

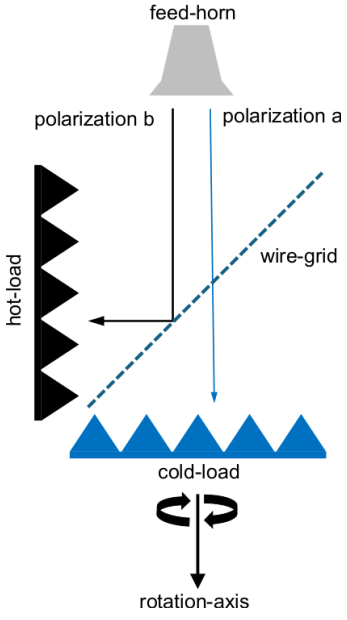

Figure 9. Measurement setup according Lahtinen et al. (2003). The wire grid is placed in a 45°deg angle in between the hot-load and cold-load. The grid rotation by the angle α is around the axis, illustrated with a black straight arrow.

https://doi.org/10.5194/egusphere-2025-2561
Preprint. Discussion started: 16 September 2025

For the grid rotation angle α, the third Stokes component for different orientations is:

$$T_v^{\alpha=0^\circ} = T_h^{\alpha=90^\circ} = T_1 \tag{23}$$

$$T_v^{\alpha=90^\circ} = T_h^{\alpha=0^\circ} = T_2 \tag{24}$$

$$T_v^{\alpha=45^\circ} = T_h^{\alpha=45^\circ} = \frac{1}{2}(T_1 + T_2) \tag{25}$$

$$T_3^{(\alpha=0^\circ,90^\circ)} = 0 \tag{26}$$

$$T_3^{(\alpha=45^\circ)} = T_1 - T_2 \tag{27}$$

$$T_4 = 0 \tag{28}$$

The cross talk coefficients $c_{a,b}$ are complex numbers and can be written as:

$$c_{a,b} = |c_{a,b}| e^{\delta_{a,b} i} \tag{29}$$

Considering the a-polarization chain, multiple measurements r_a^α with specifically chosen angles α, and a pure ambient load measurement r_a^H, were made and inserted in the following system of equations:

$$r_a^{(\alpha=0)} = |\mathscr{G}_a|^2 T_1 + |\mathscr{G}_a|^2 |c_a|^2 T_2 + n_1 \tag{30}$$

$$r_a^{(\alpha=90)} = |\mathscr{G}_a|^2 T_2 + |\mathscr{G}_a|^2 |c_a|^2 T_1 + n_1 \tag{31}$$

$$r_a^{(\alpha=45)} = \frac{1}{2}|\mathscr{G}_a|^2 \left(1 + |c_a|^2\right)(T_1 + T_2) + |\mathscr{G}_a|^2 |c_a| (T_1 - T_2)\cos(\delta_a) + n_1 \tag{32}$$

$$r_a^H = |\mathscr{G}_a|^2 \left(1 + |c_a|^2\right) T_H + n_1. \tag{33}$$

With the known brightness temperature T_1 and T_2 equations (30) - (33) can be solved for $|\mathscr{G}_a|, |\mathscr{G}_b|, |c_a|, |c_b|, \delta_a, \delta_b$. Figure 10 summarizes the obtained calibration coefficients for our receiver chain and all observations made at the laboratory at the University of Bern.

5.3 On-site calibration of instrument gain and noise

During the test campaign, we performed on-site calibrations, assuming that the crosstalk coefficients $|c_a|, |c_a|, \delta_a, \delta_b, \Delta\phi$ stayed constant. The instrument gains $|\mathscr{G}_a|^2, |\mathscr{G}_b|^2$ and instrument noise was calibrated within a cycle of 9 seconds with the internal noise diodes. The calibration cycle is to steer the mirror on the hot-target r^H for 3 seconds, switch on the noise diode for another 3 seconds (r^{H+ND}), and finally for the remaining 3 seconds, pointing towards the sky direction r^{sky}. The adapted two-point calibration equation is:

https://doi.org/10.5194/egusphere-2025-2561
Preprint. Discussion started: 16 September 2025

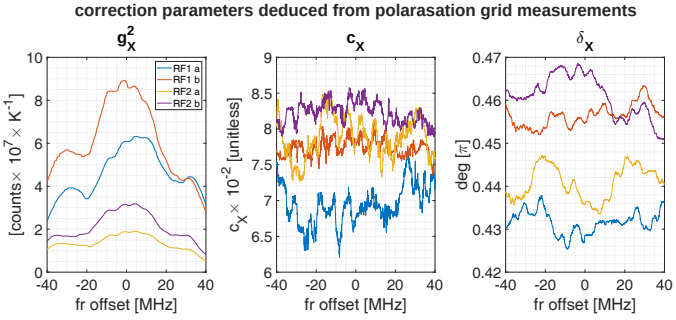

Figure 10. Crosstalk parameters calculated according Eq. (30)-(33)

$$r_a^{H+ND} = |\mathscr{G}_a|^2 (T_H + T_{ND}) + |\mathscr{G}_a|^2 |c_a|^2 T_H + n_a. \tag{34}$$

$$r_a^{H} = |\mathscr{G}_a|^2 \left(1 + |c_a|^2\right) T_H + n_a. \tag{35}$$

The calibration equation for the receiver channel b is identical. Solving for $\mathscr{G}_a$ and n_a yields:

$$|\mathscr{G}_a|^2 = \frac{r_a^{H+ND} - r_a^H}{T_{ND}} \tag{36}$$

$$n_a = \frac{T_H (r_a^H - r_a^{H+ND})(1 + |c_a|^2)}{T_{ND}} + r_a^H. \tag{37}$$

$$\tag{38}$$

The hot-target temperature T_H is constantly monitored with three temperature sensors. The noise diode temperature T_{ND} was stabilized with Peltier cooling modules and calibrated with liquid nitrogen on the first and last day of the campaign.

5.4 On-site calibration of cross-correlated parameters

Besides the normal noise temperature calibration, we also performed an evaluation of the cross-correlated parameters, considering the equation:

$$r_{3,4} = \langle \mathscr{G}_a \mathscr{G}_b^* \left(1 + c_a^* c_b\right) E_v E_h^* \rangle + \langle \mathscr{G}_a \mathscr{G}_b^* c_a E_h E_h^* \rangle + \langle \mathscr{G}_a \mathscr{G}_b^* c_b^* E_v E_v^* \rangle + o_{3,4}. \tag{39}$$

The calibration of T_3 and T_4 uses the absolute values $|\mathscr{G}_a|, |\mathscr{G}_b|$ of the instrument gain. In the next step, the complex angle $\Delta\phi$ of the combination $\mathscr{G}_a \mathscr{G}_b^*$ has to be estimated. The complex angles of the individual gains are of no importance. First, the factor $c_a^* c_b << 1$ was dropped for simplicity, and the first term on the right-hand side can be rewritten to:

$$\langle \mathscr{G}_a \mathscr{G}_b^* E_v E_h^* \rangle = |\mathscr{G}_a| |\mathscr{G}_b| \left\langle e^{i\Delta\phi} E_v E_h^* \right\rangle. \tag{40}$$

https://doi.org/10.5194/egusphere-2025-2561
Preprint. Discussion started: 16 September 2025

The instrument noise is uncorrelated (independent random noise) and, hence, zero in the cross-correlated channels. The remaining signal offset $o_{3,4}$ can be removed by subtracting the hot target spectrum. The hot target is assumed to be unpolarised, resulting in:

$$\left\langle E_v^H E_h^{H*} \right\rangle = 0. \tag{41}$$

Therefore, the difference between sky and hot-load of equation (39) is given by:

$$r_{3,4}^{sky} - r_{3,4}^{H} = |\mathscr{G}_a||\mathscr{G}_b| \left\langle e^{i\Delta\phi} E_v^{sky} E_h^{sky*} \right\rangle + R_X \tag{42}$$

with the rest term R_X, expressed by:

$$R_X = \left\langle \mathscr{G}_a \mathscr{G}_b^* \left(c_a^* \left[E_h^{sky} E_h^{sky*} - E_h^H E_h^{H*} \right] + c_b \left[E_v^{sky} E_v^{sky*} - E_v^H E_v^{H*} \right] \right) \right\rangle. \tag{43}$$

The rest term R_X appears to be very small and was fitted with the assumption that the V-Stokes is zero for frequencies that are more than 17.5 MHz away from the centre frequency, and removed from the spectrum afterwards (see Fig. 11). The complex angle $\Delta\phi$ can be estimated from the measurements of the rotatable polarizing grid (see. Sec.5.2) by making use of the relation $T_4 = 0$ for radiation passing an ideal polarization grid. This was reached by iteratively finding the zero point of the function:

$$\int_{\Delta\nu} V(\nu, \Delta\phi) d\nu = 0, \tag{44}$$

$$V(\nu, \Delta\phi) = \frac{1}{|\mathscr{G}_a||\mathscr{G}_b|} \Im \left\{ \left(r_{3,4}^{lab} - r_{3,4}^{H} \right) \mathrm{e}^{\Delta\phi i} \right\}, \tag{45}$$

where the integral covers the entire bandwidth $\Delta\nu$.

To estimate $\Delta\phi$ on the campaign site, symmetry properties of the sky measurements can be used. The V-Stokes component of the observed emission lines is anti-symmetric around the line center, while the U-Stokes component is symmetric. The complex angle $\Delta\phi$ separates the two spectra from each other. For the optimal $\Delta\phi$, the U-Stokes reaches the best symmetry, while the V-Stokes approaches the best anti-symmetry. The optimal $\Delta\phi$ can be found by separating the frequency band with bandwidth $\Delta\nu$ into two parts through the line-center frequency ν_c, and defining a norm N_V for example by:

$$N_V(\Delta\phi) = \sqrt{\int_0^{\Delta\nu/2} \left[V(\nu_c + \nu, \Delta\phi) - V(\nu_c - \nu, \Delta\phi) \right]^2}, \tag{46}$$

$$V(\nu, \Delta\phi) = \frac{1}{|\mathscr{G}_a||\mathscr{G}_b|} \Im \left\{ \left(r_{3,4}^{sky} - r_{3,4}^{H} \right) \mathrm{e}^{\Delta\phi i} \right\}. \tag{47}$$

https://doi.org/10.5194/egusphere-2025-2561
Preprint. Discussion started: 16 September 2025

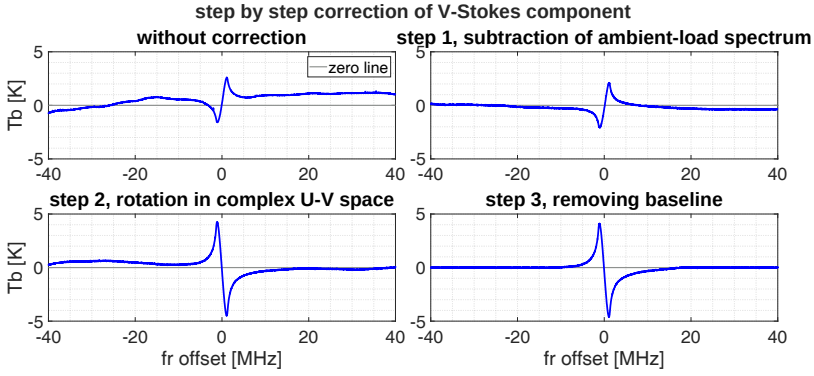

Figure 11. Step-by-step correction of the V-Stokes component. The second panel is after subtracting $r^H_{3,4}$, and the third panel is after rotating by $\Delta\phi$. In the last step, R_X is removed by interpolation.

The angle with the highest anti-symmetry is where the maximum of N_V is located. With this method, the optimal angle was $\Delta\phi = 0.65 \pm 0.01\pi$ rad while the same coefficient estimated with the polarized grid was $\Delta\phi = 0.64 \pm 0.01\pi$ rad. After estimating $\Delta\phi$, the two Stokes components T_3 and T_4 can be calculated to:

$$T_3^{sky} = \frac{2}{|\mathscr{G}_a||\mathscr{G}_b|}\Re\left\{\left(r_{3,4}^{sky} - r_{3,4}^{H}\right)\mathrm{e}^{\Delta\phi i} - R_X\right\} \tag{48}$$

$$T_4^{sky} = \frac{2}{|\mathscr{G}_a||\mathscr{G}_b|}\Im\left\{\left(r_{3,4}^{sky} - r_{3,4}^{H}\right)\mathrm{e}^{\Delta\phi i} - R_X\right\}. \tag{49}$$

The function $N_V(\Delta\phi)$ and $T_{sky,4}$ spectra for different $\Delta\phi$ are illustrated in Fig. 12. The full set of calibrated Stokes components, together with the corresponding instrument noise, is illustrated in Fig. 13.

5.5 On-site calibration of self-correlated parameters

Finally, we also investigated the campaign calibration for self-correlated parameters to correct the sky measurements substituting the previously obtained calibration results into Eq. (15)

$$r_a = |\mathscr{G}_a|^2 T_{sky,v} + |\mathscr{G}_a|^2|c_a|^2 T_{sky,h} + |\mathscr{G}_a|^2|c_a|\Re\left\{(T_{sky,3} + T_{sky,4}i)\,e^{\delta_a i}\right\} + n_a \tag{50}$$

Since $|c_b|^2 << 1$, the second term on the right-hand side was dropped for simplicity, leading to:

$$\frac{r_a - n_a}{|\mathscr{G}_a|^2} - |c_a|\left[T_{sky,3}\cos(\delta_a) - T_{sky,4}\sin(\delta_a)\right] = T_{sky,v} \tag{51}$$

The first term on the left-hand side is the uncorrected brightness temperature, and the second term is the correction term. $T_{sky,3}$ and $T_{sky,4}$ where corrected beforehand (see Section 5.4). The effect of subtracting the correction term is illustrated in Fig. 14.

https://doi.org/10.5194/egusphere-2025-2561
Preprint. Discussion started: 16 September 2025

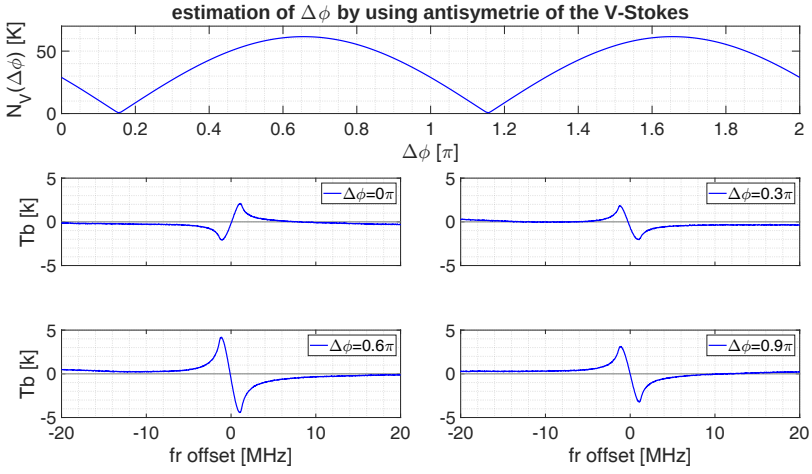

Figure 12. Upper panel: N_V as in Eq. (46) as a function of $\Delta\phi$.
Bottom panels: Calibrated T_4^{sky} spectrum (Eq. (49)) using different values for $\Delta\phi$. The U- and V- Stokes components mix differently depending on $\Delta\phi$.

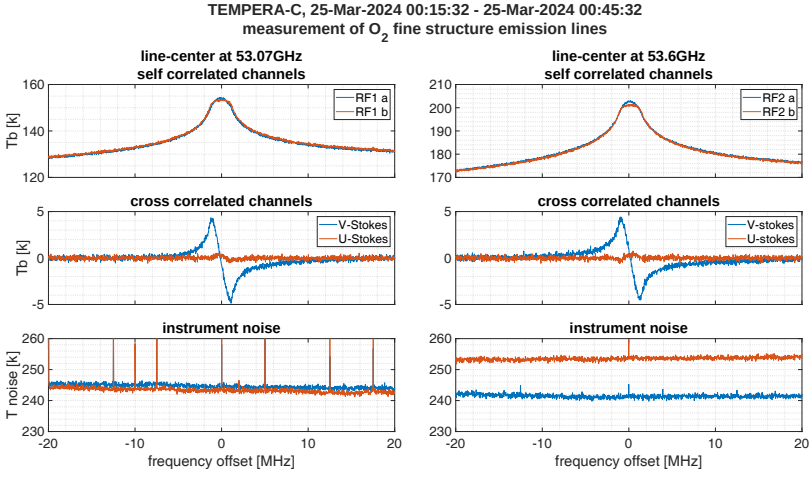

Figure 13. TEMPERA-C calibrated and corrected spectra and instrument noise temperatures measured at the high altitude research station.

The uncorrected line spectrum has a small asymmetry generated by the contribution of $|c_a|T_{sky,4}\sin(\delta_a)$ since this spectrum is antisymmetric around the line centre. This asymmetry can be removed by subtracting the correction term.

The onsite calibration was performed with the built-in noise diodes within a calibration circle of 9 seconds. The noise equivalent differential temperature (NEDT) after 30 min integration is in the range $\Delta T_{v,h}$ = 0.24±0.005 K for the self-correlated components and $\Delta T_{v,h}$ = 0.16±0.004 K for the cross-correlated components. Between $T_{sky,v}$ and $T_{sky,h}$ a bias was found with magnitude in a range identical to the NEDT. This bias was not constant and frequently even changed sign. However, this is not critical for the retrievals, since the combination $T_{LCP,RCP} = \frac{1}{2}(T_v + T_h) \pm T_3$ cancels the offset.

https://doi.org/10.5194/egusphere-2025-2561
Preprint. Discussion started: 16 September 2025

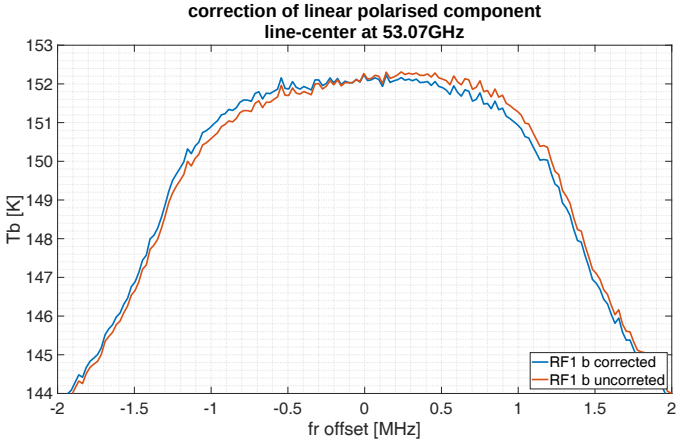

Figure 14. $T_{sky,v}$ before and after correction according (51). The uncorrected line spectrum shows an asymmetry around the line center, which is removed after applying the correction.

6 The inversion algorithm

The forward model and retrieval were simulated with ARTS 2.6 Buehler et al. (2024) using the interface for Python. The mathematical formalism is from Rodgers (2000). For an atmospheric state vector x, the forward model F gives a spectrum y:

$$y = F(x, b) + \epsilon \tag{52}$$

For normal distributed random variables (x, y) and the usage of Bayes theorem, the x maximizing the density function $P(x|y)$ (probability to measure x under the condition that y is known) minimizes the cost function:

$$J(x) = [y - F(x)]^T \mathbf{S}_\epsilon^{-1} [y - F(x)] + [x - x_a]^T \mathbf{S}_a^{-1} [x - x_a] . \tag{53}$$

The minimum of the cost function can be found by computing the x for which the gradient of the cost function becomes zero:

$$\nabla_x J(x) = 0. \tag{54}$$

x_a is the apriori profile, S_a the apriori error covariance matrix, and S_e is the measurement error covariance matrix. The local minimum of the cost function is calculated by iteratively decreasing its gradient using the Levenberg-Marquardt algorithm:

$$x_{i+1} = x_i + \left(\mathbf{S}_a^{-1} + \mathbf{K}_i^T \mathbf{S}_\epsilon^{-1} \mathbf{K}_i + \gamma \mathbf{I}\right)^{-1} \left[\mathbf{K}_i^T \mathbf{S}_\epsilon^{-1} (y - F(x_i)) - \mathbf{S}_a^{-1} (x_i - x_a)\right] . \tag{55}$$

$\mathbf{K}$ is the forward model Jacobian, also called the weighting function, defined as:

https://doi.org/10.5194/egusphere-2025-2561
Preprint. Discussion started: 16 September 2025

$$\mathbf{K} = \frac{\partial y}{\partial x}. \tag{56}$$

The model is set up in stratified atmosphere on a 10×10 latitude-longitude grid with the dimensions 0.2°×0.2°. The altitude grid has a grid spacing of 1km and ranges from 0-70 km. Apriori temperature and water vapour profiles are constructed by using a long-time average of ECMWF profiles. The Oxygen VMR is set to a constant value of 21%. The zenith angle is 30° (60° elevation). The Zeeman broadening effect is implemented for radiative transfer simulations in the middle atmosphere Larsson et al. (2019); Krochin et al. (2022b). For the Earth's magnetic field, the IGRF model is implemented in ARTS.

In the troposphere, the Line-Mixing effect is considered next to pressure broadening. In previous versions of ARTS, Line-Mixing could not be used in the Oxygen band, and a tropospheric correction was performed instead of direct radiative transfer simulations. In the current retrieval version, the troposphere is included in the forward model. For temperature sensing in the middle atmosphere, the tropospheric temperature profile does not need to be known exactly since only the total tropospheric opacity is important. This opacity is dominated by the lowest few kilometers in the troposphere. In our forward model, we take the values for surface temperature, pressure, and humidity from the Jungfrau Ostgrat weather station (the distance between the Sphinx Observatory and the Ostgrat station is 650 m with 240 m difference in altitude). For the apriori profile, the values at the measurement platform are linearly extrapolated using the grid point from ECMWF at 4 km and the measurements from the Ostgrat station. A remaining baseline offset is handled with a baseline correction retrieval. With this method, the tropospheric opacity is estimated more accurately compared to the previous correction (Ingold and Kämpfer (1998)), but the retrieved profiles in the troposphere are idealized and not suitable for higher-level data products.

The forward model is simulated by pencil beam calculations and constant channel response, as no sensor characteristics were implemented. Instrument noise was assumed constant for each channel, and the channels were treated as independent. The measured channel noise is around $\Delta T_a = 0.2-0.3$ K with small differences between the receiver chains. The apriori covariance matrix S_a has constant diagonal values σ_a^2 for all altitudes. The covariance for off-diagonal elements was calculated with:

$$S_{a(ij)} = \sigma_a^2 \exp\left(\frac{|z_i - z_j|}{z_c}\right) \tag{57}$$

where the correlation length was chosen to $z_c = 1$ km.

7 The advantage of polarimetric measurements

In this section we investigate whether the information gain due to the fully polarimetric approach has an impact on the temperature retrieval. For this purpose, we compare the altitude resolution and measurement response vector between retrievals performed with a single total intensity spectrum and two circularly polarized spectra obtained by simulations and measure-

https://doi.org/10.5194/egusphere-2025-2561
Preprint. Discussion started: 16 September 2025

ments.

Assuming a standard atmosphere as a reference case, an atmospheric spectrum was simulated by running the forward model for a certain state space vector x_f. After adding normally distributed noise, the spectrum was inverted using the same forward model, where the apriori state was set with an offset Δx from the initial state vector $x_a = x_f + \Delta x$. This routine was performed with the total intensity spectrum and also with the two circularly polarized states. Compared to the retrieval algorithm with measurements, this set-up is an idealization since the measurement vector is produced by the model atmosphere and, therefore, is unbiased against the forward model. For this reason, the baseline retrieval was not part of the retrieval quantities in this configuration. The altitude resolution and measurement response of both retrievals are compared in Fig. 15. In this specific case, the instrument noise was set to $\sigma_e = 0.2$ K and the apriori error $\sigma_a = 30$ K. For the offset vector Δx, a Gaussian function was chosen with a peak of $\Delta x_{max} = 6$ K at 50 km and a cutoff for values above 8 km from the peak. The altitude resolution of the polarimetric retrieval is slightly higher by roughly 3-6% above 35 km. A small stretch is visible in the measurement response profile, but it seems insignificant. Different combinations of $\sigma_e, \sigma_a, \Delta x$ were tested, but no combination with more significant differences was found. The error and offset parameters used for the ideal case study were $\sigma_e = [0.1, 0.2, 0.4, 0.8]$ K,$\sigma_a = [24, 28, 30]$ K and offset values of $\Delta x_{max} = [-10, -6, -3, 0, 3, 6, 10]$ K. The increase in altitude resolution of the polarimetric retrievals between 35-70 km was, on average 4.7$\pm$0.5% without clear dependence on the retrieval parameters. The absolute altitude resolution is higher for lower instrument noise in all cases. Altitudes with MR = 1 were between 68-69 km for the lowest instrument noise and 63-64 km for the highest. In about half of the cases, this altitude was one grid point higher in the polarimetric retrieval and equal to total intensity retrieval in the rest of the cases. Therefore, the altitude grid spacing of 1 km can be seen as an upper boundary for the increase of the upper altitude range for polarimetric retrievals compared to total intensity retrievals.

$\sigma_a \backslash \sigma_e$ [K]	0.1	0.2	0.4	0.8
24	5.1/8.2/13.6	5.6/9.1/14.6	6.2/10.3/10.3	6.9/11.3/16.5
28	5.1/8.0/13.4	5.4/8.9/14.3	6.1/10.0/15.1	6.6/10.9/16.2
30	5.1/8.0/13.3	5.5/8.9/14.3	6.0/9.9/15.1	6.6/10.9/ 16.1

Table 1. Altitude resolution total intensity retrieval min/mean/max [km]

$\sigma_a \backslash \sigma_e$ [K]	0.1	0.2	0.4	0.8
24	5.1/7.6/13.0	5.6/8.4/14.1	6.2/9.3/15.0	6.7/10.3/16.1
28	5.1/7.5/12.8	5.5/8.2/13.9	6.0/9.1/14.8	6.6/10.1/15.7
30	5.0/7.4/12.8	5.5/8.1/13.7	6.0/9.0/14.7	6.6/10.0/15.6

Table 2. Altitude resolution circular polarization retrieval min/mean/max [km]

https://doi.org/10.5194/egusphere-2025-2561
Preprint. Discussion started: 16 September 2025

$\sigma_a \backslash \sigma_e$ [K]	0.1	0.2	0.4	0.8
24	4.56	4.38	4.74	4.45
28	4.77	4.73	4.94	5.18
30	4.69	4.65	5.00	5.22

Table 3. Relative increase (%) in altitude resolution retrieving two circular polarized spectra compared to one total intensity spectrum.

$\sigma_a \backslash \sigma_e$ [K]	0.1	0.2	0.4	0.8
24	68/69	67/68	66/66	63/64
28	69/69	68/68	66/67	64/65
30	69/69	68/68	66/67	64/65

Table 4. Upper altitude limits [km] of total polarization / circular polarization retrievals

In Krochin et al. (2022b), we have argued that the upper altitude limit of temperature retrievals can be increased by using polarimetric measurements compared to single-polarization measurements. The argument was that the increased information content could compensate for the Zeeman broadening, which dominates at lower pressures. However, our retrieval test case designed with a synthetic idealized atmospheric profile, shown in this manuscript, indicates that the upper altitude limit can be slightly improved by using fully polarimetric retrieval in comparison to total intensity retrievals, but the main improvement is mostly due to the updated version of ARTS and improved retrieval algorithm. In Krochin et al. (2022a), the upper altitude limit for temperature retrievals of TEMPERA was 50 km. The retrieval was performed with the tropospheric correction, and the ARTS version used in this study was ARTS 2.4. The ARTS version used in the current study is 2.6, which has updated Zeeman splitting coefficients and implemented line-mixing calculation. Also, the instrument noise of TEMPERA was higher than in the current study. In earlier ideal case studies, the instrument noise of the total intensity retrieval was also not reduced by a factor of $\sqrt{2}$. Retrieving the right and left circular polarized spectra, both with a constant channel noise of σ_e, the effective noise is $\frac{1}{\sqrt{2}}\sigma_e$ because two independent measurements are used. This has to be taken into account when comparing retrievals with one against multiple spectra. In this study when the channel noise σ_e was used for the polarimetric retrievals then the channel noise $\frac{1}{\sqrt{2}}\sigma_e$ was used for the total intensity retrieval.

Even though the gain in altitude range and altitude resolution in this case study is smaller than expected, fully polarimetric measurements are still of use for ground-based remote sensing. By simultaneously measuring two polarization states, the instrument noise is reduced by a factor of $\sqrt{2}$. This also means a reduction of integration time by a factor of 2 for the same instrument noise compared to single-polarization instruments. An additional advantage of fully polarized measurements, compared to linear polarized ones, is that in the case where only the two linear polarizations are measured, the polarization plane has to be known in the retrieval algorithm. This is because the Zeeman broadened Q-Stokes spectrum does not vanish. The polarization plane can rotate when mirrors are used to guide the atmospheric signal into the receiver, which makes it difficult

https://doi.org/10.5194/egusphere-2025-2561
Preprint. Discussion started: 16 September 2025

to determine and is a potential source of errors. Whereas for circular polarization receiver chains with cross-correlation, the polarization plane does not matter.

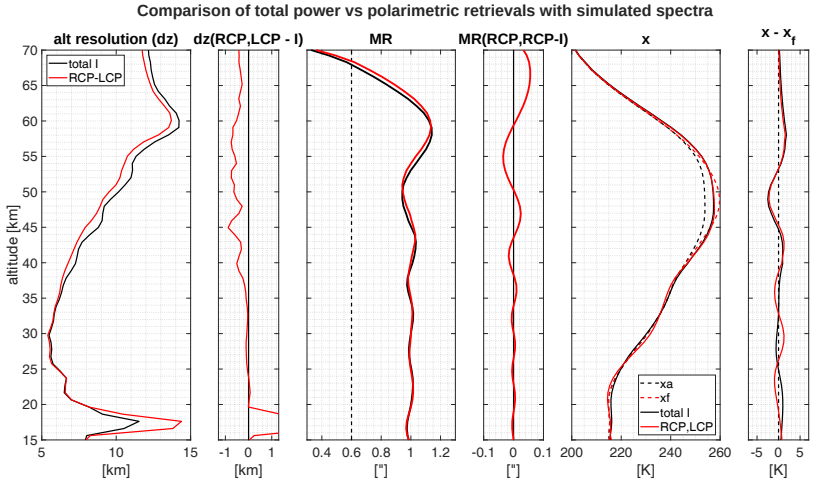

Figure 15. Results of the comparison with idealized conditions where the retrieval algorithm was run with simulated spectra. The plot shows the altitude resolution, measurement response, retrieved, and a priori temperature profiles.

8 Results

8.1 Retrieval performance

For the inversion of the measurements, the apriori error was set constant to $\sigma_a = 30$ K for all altitudes and the measurement error to $\sigma_e = 0.5$ K for all channels. Lower values for the measurement error lead to convergence problems. This is usually the case because systematic offsets and forward model errors are not covered by the measurement error. The retrieved temperature profiles have an effective altitude range (range where the measurement response is above 0.6), of 20-60 km and an altitude resolution (defined by the FWHM of the averaging kernels rather than by the vertical grid of the atmospheric profile) below 15 km within this range. Between 25-40 km, the altitude resolution is even below 10 km.

Remaining systematic residua were found in the RCP spectra, as well as a small numerical oscillation in the temperature profile around 40 km (see Fig.16). We assume that the characteristic residuum is an artifact from the calibration process, as it appears to be a fraction of the V-Stokes component and only shows in one of the polarizations. Residua caused by the initialization of the forward model should appear in both polarizations. The small oscillation in the temperature is related to a convergence issue. Preventing the retrieval from convergence into a state space vector without oscillations was a general challenge, where many different convergence criteria were tried. Performing the retrieval with only one of the two emission lines showed a much better convergence towards a plausible state space vector. We, therefore, assume that the convergence issue is due to a baseline

https://doi.org/10.5194/egusphere-2025-2561
Preprint. Discussion started: 16 September 2025

offset between the measured emission lines in combination with the baseline retrieval, which requires retrieving one baseline covering both lines. Retrieved baseline offsets were in the range of 6-10 K. Possible reasons are uncertainties in the lowest levels of the model atmosphere and radiative transfer and biases of the calibration target temperatures.

For a comparison, the same retrieval algorithm was used to invert the total intensity spectrum. The direct comparison of the inversions of the total intensity spectrum against the circularly polarized spectra are shown in Fig. 17. This procedure results in the retrieval of two circularly polarized states that involve two independent spectra, and the effective measurement error is reduced by a factor of $\sqrt{2}$. To compare the pure effect of the different polarization states, the measurement error of the total intensity spectrum was divided by $\sqrt{2}$. This ensures that the difference in the retrieval results is only due to the different information in the polarization states and is not due to the reduced noise by using two independent measurements (right and left circular polarization). The comparison shows a higher altitude resolution in the polarimetric retrievals of 8% on average. Between 40-50 km, the difference is even above 10%. The measurement response is of similar magnitude, but a vertical stretch was found in the polarimetric case. The upper altitude limit is also in a comparable range, with 61 km for the total intensity and 63 km for the polarimetric retrieval. In the retrieved profiles, the absolute difference can reach up to 5 K.

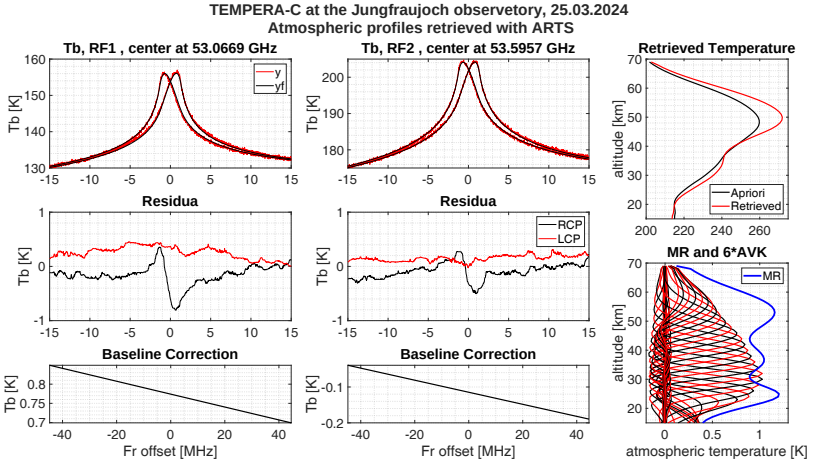

Figure 16. Retrieval result overview for a single measurement. Remaining residues in the RCP spectra are mainly due to calibration uncertainties.

8.2 Continuous temperature series

The Instrument was deployed as a breadboard to the Sphix observatory and performed a continuous temperature measurement covering the period from 25.03.2024 to 12.11.24. The level 1 dataset contains data gaps due to electricity cut-offs. Additional data gaps in the level 2 data are due to weather conditions. At 3571 m altitude, snowfall frequently disturbs the measurements. While during light snowfall, temperature retrievals were occasionally possible, spectra measured during heavy snowfall did not contain enough stratospheric signal to be analyzed. Also, accumulation of snow and ice particles on the microwave window

https://doi.org/10.5194/egusphere-2025-2561
Preprint. Discussion started: 16 September 2025

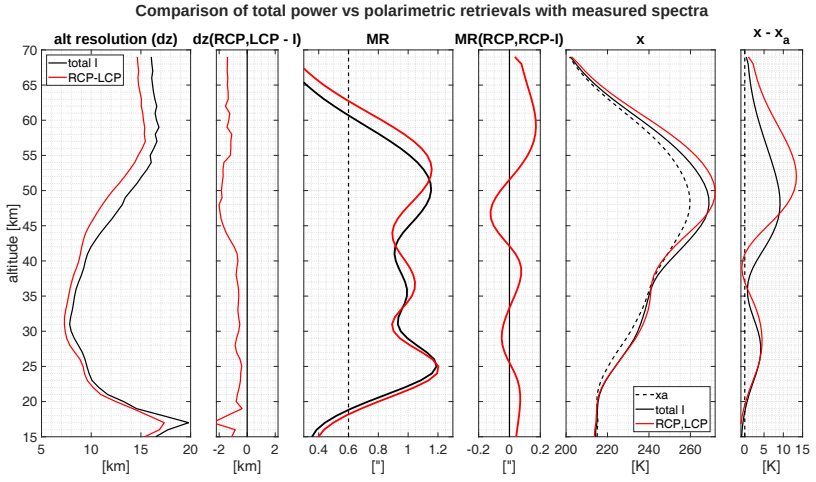

Figure 17. Results of the comparison with real conditions where the retrieval algorithm was run with measured spectra. The plot shows the altitude resolution, measurement response, retrieved and apriori temperature profiles.

affected the instrument performance. We assume that frost formation and wetting of the microwave transparent window were major causes for disturbed measurements during these weather conditions. During easterly wind conditions (frontal on the window), it was found that the chance for disturbances was higher than when the wind came from other directions. Ice particles and snowfall can have different effects on the polarization of the received radiation, which has to be further investigated. Other weather conditions disturbing the measurements were, as usual, heavy cloud coverage and rainfall. The temperature profile time series is illustrated in Fig. 18. Towards the end of August, the LO had reset after a power cut-off and had to be reprogrammed on site, preventing the collection of data for the rest of the month.

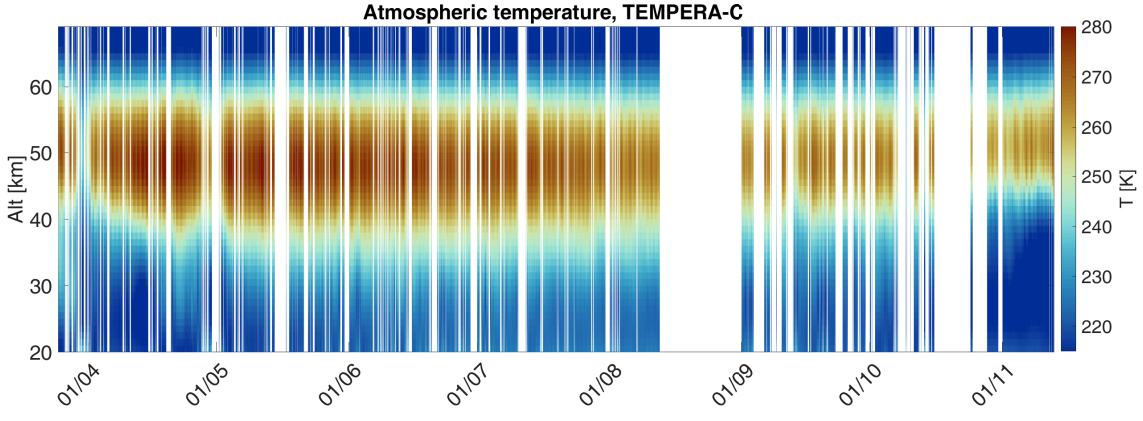

Figure 18. Series of the profiles of retrieved atmospheric temperature during the Jungfraujoch campaign. The data gaps are explained in the text. The dataset of retrieved temperature profiles shows dynamical features, such as thermal tides.

https://doi.org/10.5194/egusphere-2025-2561
Preprint. Discussion started: 16 September 2025

9 Discussion

In this manuscript, we have shown that a digital correlating radiometer can be calibrated without using a phase-retardation plate and that the U and V Stokes components can be calibrated on-site with a simple two-point calibration, provided the spectra fulfil symmetry properties. The remaining uncertainties in the calibration results are mainly due to the non-ideal performance of the polarized grid since we have neglected the grid coefficients $t_\perp, r_\parallel, r_l$ in our laboratory calibration. Also, tuning the grid rotation angle was difficult. We assume that these uncertainties cause the characteristic shape of the retrieval residua of the right-circular components. Crosstalk parameters were assumed to stay constant during the campaign. A comparison of calibrated spectra during calm weather conditions at the beginning and the end of the campaign did not reveal any significant differences apart from such due to different atmospheric states.

The results of the retrieval algorithm show an effective altitude range of 20-60 km. A direct comparison of retrievals with spectra of total polarization against circular polarization showed an increase in altitude resolution of about 8% on average in the effective altitude range and upper altitude limit of about 2 km in the polarimetric case. The improvement compared to single-polarization retrievals is, however, less than expected. Other advantages of fully polarimetric instruments are that the integration time can be reduced by a factor of 2 and that the rotation of the polarization plane in the optics does not need to be determined because circular polarization does not depend on the polarization plane.

Besides strong precipitation, the wind direction had a big influence on the measured spectra. We assume that wetting and frosting of the microwave transparent window has the biggest effect in changing the polarization state. However, data has yet to be validated and further analyzed to fully understand the influence of different weather conditions and the microwave transparent window.

The test campaign was conducted at a fixed azimuth direction. For future observations, it is important to investigate the change in lineshape for different angles to the magnetic field. Meanwhile TEMPERA-C is integrated into a weather-proofed housing and undergoes environmental testing at the University of Bern at 550 m.a.s.l. Once these tests are completed TEMPERA-C will be redeployed on the outside platform of the Sphinx laboratory in 2025. The outdoor platform is suitable for TEMPERA-C to perform systematic azimuthal scans. This new data provides a pathway for magnetic field retrievals using the Stokes components for all azimuth beams.

10 Conclusion

In this study, we present theoretical calculations implementing a state-of-the-art atmospheric radiative transfer model and laboratory measurements to calibrate a fully polarimetric radiometer. We demonstrate all steps of the simplified calibration procedure and evaluate crosstalk-coefficients to obtain all four Stokes components for two oxygen emission lines at 53.067 and 53.596 GHz. A polarizing wire grid in combination with unpolarized hot and cold targets were used to determine the crosstalk

https://doi.org/10.5194/egusphere-2025-2561
Preprint. Discussion started: 16 September 2025

between the receiver channels and to assess asymmetries in the receiver chains for each polarization. We have also shown how the measured spectra of the U and V-Stokes components of the Zeeman affected emission lines can be used to fine-tune one of the crosstalk parameters.

The laboratory calibration results are applied to observations conducted with a breadboard setup of the new TEMPERA-C instrument. We analyzed the measurements with a new retrieval algorithm, including the latest update to Zeeman line splitting in ARTS. Our retrieval also accounts for line mixing effects, altering the baseline of each spectral line for the temperature retrieval. Furthermore, the new algorithm omits a classical tropospheric correction and estimates the tropospheric opacity directly from reanalysis data. The biggest advantage of the new retrieval compared to previous versions presented in Krochin et al. (2024), is the information gain due to the separation of left and right-hand circular polarization, which results in twice the temporal resolution. The extension of the altitude coverage at which temperatures can be retrieved results in 4-5 km compared to older retrieval versions.

During a test campaign at the Jungfraujoch high-altitude research station at the Sphinx observatory at an altitude of 3571 m, we performed several on-site calibrations and evaluated the stability of our laboratory calibration coefficients. The data quality obtained during the test campaign also highlighted the benefit of a high altitude station by increasing the signal strength of the observed emission lines by a factor of 4. We recorded a nearly continuous time series of 8 months with our breadboard setup. Data gaps were mostly due to snow and water accumulation at the microwave window and due to power outages of the station due to ongoing constructions.

https://doi.org/10.5194/egusphere-2025-2561
Preprint. Discussion started: 16 September 2025

Appendix A: Appendix 1: Retrieval error quantities

A widely used quantifier of the retrieval algorithm is the averaging kernel matrix defined by:

$$\mathbf{A} = \mathbf{GK}. \tag{A1}$$

Where G is the Jacobian of the inverse model $\hat{x} = F^{-1}(y)$, also called gain matrix or contribution function:

$$\mathbf{G} = \frac{\partial \hat{x}}{\partial y}. \tag{A2}$$

The altitude resolution of the retrieval algorithm can be estimated with the full-width-at-half-maximum of the rows of $\mathbf{A}$. The weighted sum over the rows of $\mathbf{A}$ is the measurement response:

$$mr_i = \frac{\mathbf{A}_i x_a}{x_{ai}}. \tag{A3}$$

The observational error covariance matrix $\mathbf{S}_o$ is defined by mapping the measurement covariance matrix $\mathbf{S}_\epsilon$ into the state space:

$$\mathbf{S}_o = \mathbf{G}\mathbf{S}_\epsilon\mathbf{G}^T. \tag{A4}$$

Weighting the apriori covariance matrix $\mathbf{S}_a$ with the averaging kernel gives the smoothing error caused by the finite resolution of the observation system:

$$\mathbf{S}_s = (\mathbf{A} - \mathbf{I})\,\mathbf{S}_a\,(\mathbf{A} - \mathbf{I})^T. \tag{A5}$$

Author contributions. WK developed the calibration scheme, performed the calibration, implemented the retrieval and the data analysis of TEMPERA-C observations. WK and GS conceptualized the content of the manuscript. AM guided and supported the preparation of the paper. All authors contributed to the editing of the manuscript.

Competing interests. The authors declare that they have no competing interests.

Acknowledgements. This research has been supported by the Schweizerischer Nationalfonds zur Förderung der Wissenschaftlichen Forschung (grant no. 200021-200517 / 1), and the Swiss Polar Institute (SPI) supports the development of the TEMPERA-C radiometer. We would like

https://doi.org/10.5194/egusphere-2025-2561
Preprint. Discussion started: 16 September 2025

to thank the International Foundation High Altitude Research Stations Jungfraujoch and Gornergrat (HFSJG), 3012 Bern, Switzerland, for enabling us to carry out our experiments at the Jungfraujoch High Altitude Research Station. We thank the ARTS developer team for their support and Richard Larsson for implementing the Zeeman and Line-Mixing effect in ARTS. Scientific color maps (Crameri et al., 2020) are used in this study to prevent visual distortion of the data and exclusion of readers with color-vision deficiencies.

https://doi.org/10.5194/egusphere-2025-2561
Preprint. Discussion started: 16 September 2025

References

Buehler, S. A., Eriksson, P., Kuhn, T., von Engeln, A., and Verdes, C.: ARTS, the Atmospheric Radiative Transfer Simulator, Journal of Quantitative Spectroscopy and Radiative Transfer, 91(1), 65–93, https://doi.org/10.1016/j.jqsrt.2004.05.051, 2005.

Buehler, S. A., Mendrok, J., Eriksson, P., Perrin, A., Larsson, R., and Lemke, O.: ARTS, the Atmospheric Radiative Transfer Simulator – version 2.2, the planetary toolbox edition, Geoscientific Model Developement, 11, 1537–1556, https://doi.org/10.5194/gmd-11-1537-2018, 2018.

Buehler, S. A., Larsson, R., Lemke, O., Pfreundschuh, S., Brath, M., Adams, I., S. Fox, F. R., Czarnecki, P., and Eriksson, P.: The Atmospheric Radiative Transfer Simulator ARTS, Version 2.6 — Deep Python Integration, Journal of Quantitative Spectroscopy and Radiative Transfer, Preprint, https://doi.org/10.2139/ssrn.4815661, 2024.

Crameri, F., Shephard, G. E., and Heron, P.: The misuse of colour in science communication, Nature Communications, 11, https://doi.org/10.1038/s41467-020-19160-7, 2020.

Eriksson, P., Buehler, S. A., Kuhn, T., von Engeln, A., and Verdes, C.: ARTS, the atmospheric radiative transfer simulator, Version 2, Journal of Quantitative Spectroscopy and Radiative Transfer, 112, 1551–1558, https://doi.org/10.1016/j.jqsrt.2011.03.001, 2011.

Gasiewski, A. J. and Kunkee, D. B.: Calibration and Applications of Polarization-Correlating Radiometers, IEEE Transactions on Microwave Theory and Techniques, 41, 767–773, https://doi.org/10.1109/22.234509, 1993.

Ingold, T. and Kämpfer, N.: Weighted mean tropospheric temperature and transmittance determination at millimeter-wave frequencies for ground-based applications, Radio Science, 22, 905–918, https://doi.org/10.1029/98RS01000, 1998.

Krochin, W., Navas Guzmán, F., Kuhn, D., Murk, A., and Stober, G.: Continuous temperature soundings at the stratosphere and lower mesosphere with a ground-based radiometer considering the Zeeman effect, Atmospheric Measurement Techniques, 15, 2231–2249, https://doi.org/10.5194/amt-15-2231-2022, 2022a.

Krochin, W., Stober, G., and Murk, A.: Development of a Polarimetric 50-GHz Spectrometer for Temperature Sounding in the Middle Atmosphere, IEEE Journal of selected topics in applied earth observations and remote sensing, 15, https://doi.org/10.48350/186172, 2022b.

Krochin, W., Stober, G., and Murk, A.: Thermal tides in the middle atmosphere at mid-latitudes measured with a ground-based microwave radiometer, Atmospheric Measurement Techniques, 17, 5015–5028, 2024, https://doi.org/10.5194/amt-17-5015-2024, 2024.

Lahtinen, J., Gasiewski, A., Klein, M., and Corbella, I.: A calibration method for fully polarimetric microwave radiometers, IEEE Transactions on Geoscience and Remote Sensing, 4, 588 – 602, https://doi.org/10.1109/TGRS.2003.810203, 2003.

Larsson, R., Buehler, S. A., Eriksson, P., and Mendrok, J.: A treatment of the Zeeman effect using Stokes formalism and its implementation in the Atmospheric Radiative Transfer Simulator (ARTS), Journal of Quantitative Spectroscopy and Radiative Transfer, 133, 445–453, https://doi.org/10.1016/j.jqsrt.2013.09.006, 2014.

Larsson, R., Lankhaar, B., and Eriksson, P.: Updated Zeeman effect splitting coefficients for molekular oxygen in planetary applications, Geoscientific Model Developement, 224, 431–438, https://doi.org/10.1016/j.jqsrt.2018.12.004, 2019.

Laursen, B. and Skou, N.: Wind Direction over the Ocean Determined by an Airborne, Imaging, Polarimetric Radiometer System, IEEE Transactions on Geoscience and Remote Sensing, 39, 1547 – 1555, https://doi.org/10.1109/36.934086, 2001.

Navas-Guzmán, Kämpfer, N., Murk, A., Larsson, R., Buehler, S. A., and Eriksson, P.: Zeeman effect in atmospheric O_2 measured by ground-based microwave radiometry, Atmospheric Measurement Techniques, 8, 1863–1874, https://doi.org/10.5194/amt-8-1863-2015, 2015.

https://doi.org/10.5194/egusphere-2025-2561
Preprint. Discussion started: 16 September 2025

Piepmeier, J. R. and Gasiewski, A. J.: Digital Correlation Microwave Polarimetry: Analysis and Demonstration, IEEE Transactions on Geoscience and Remote Sensing, 39, 2392 – 2410, https://doi.org/10.1109/36.964976, 2001a.

Piepmeier, J. R. and Gasiewski, A. J.: High-resolution passive polarimetric microwave mapping of ocean surface wind vector fields, IEEE Transactions on Geoscience and Remote Sensing, 39, 606–622, https://doi.org/10.1109/36.911118, 2001b.

Rodgers, C. D.: Inverse Methods for Atmospheric sounding Theory and Practice, World Scientific, https://doi.org/doi.org/10.1142/3171, 2000.

Stähli, O., Murk, A., Kämpfer, N., Mätzler, C., and Eriksson, P.: Microwave radiometer to retrieve temperature profiles from the surface to the stratopause, Atmospheric Measurement Techniques, 6, 2477–2494, https://doi.org/10.5194/amt-6-2477-2013, 2013.